



Effects of radius ratio on annular centrifugal Rayleigh–Bénard convection

Dongpu Wang¹, Hechuan Jiang^{1,2,†}, Shuang Liu^{1,3}, Xiaojue Zhu⁴ and Chao Sun^{1,5,†}

¹Center for Combustion Energy, Key Laboratory for Thermal Science and Power Engineering of MoE, and Department of Thermal Engineering, Tsinghua University, Beijing 100084, PR China

²Huaneng Clean Energy Research Institute, Beijing 102209, PR China

³Yau Mathematical Sciences Center, Tsinghua University, Beijing 100084, PR China

⁴Max Planck Institute for Solar System Research, Justus-von-Liebig-Weg 3, Göttingen 37077, Germany

⁵Department of Engineering Mechanics, School of Aerospace Engineering, Tsinghua University, Beijing 100084, PR China

(Received 7 April 2021; revised 23 August 2021; accepted 6 October 2021)

We report on a three-dimensional direct numerical simulation study of flow structure and heat transport in the annular centrifugal Rayleigh–Bénard convection (ACRBC) system, with cold inner and hot outer cylinders corotating axially, for the Rayleigh number range $Ra \in [10^6, 10^8]$ and radius ratio range $\eta = R_i/R_o \in [0.3, 0.9]$ (R_i and R_o are the radius of the inner and outer cylinders, respectively). This study focuses on the dependence of flow dynamics, heat transport and asymmetric mean temperature fields on the radius ratio η . For the inverse Rossby number $Ro^{-1} = 1$, as the Coriolis force balances inertial force, the flow is in the inertial regime. The mechanisms of zonal flow revolving in the prograde direction in this regime are attributed to the asymmetric movements of plumes and the different curvatures of the cylinders. The number of roll pairs is smaller than the circular roll hypothesis as the convection rolls are probably elongated by zonal flow. The physical mechanism of zonal flow is verified by the dependence of the drift frequency of the large-scale circulation (LSC) rolls and the space- and time-averaged azimuthal velocity on η . The larger η is, the weaker the zonal flow becomes. We show that the heat transport efficiency increases with η . It is also found that the bulk temperature deviates from the arithmetic mean temperature and the deviation increases as η decreases. This effect can be explained by a simple model that accounts for the curvature effects and the radially dependent centrifugal force in ACRBC.

Key words: turbulent convection, turbulence simulation, rotating turbulence

† Email addresses for correspondence: jhcthu@foxmail.com, chaosun@tsinghua.edu.cn

1. Introduction

Turbulent convection is ubiquitous in nature and in many industrial processes. Examples include the convective flows in the Earth's mantle (Mckenzie, Roberts & Weiss 1974) and outer core (Cardin & Olson 1994), in the atmospheric motion (Wyngaard 1992; Hartmann, Moy & Fu 2001), in the ocean (Cheng *et al.* 2019) and in rotational machines (Michael Owen & Long 2015). Many of these convection phenomena occur under rapid rotation of the system (Bohn *et al.* 1995). Rayleigh–Bénard convection (RBC), a fluid layer heated from below and cooled from above, is a classical and idealized paradigm for the study of thermally driven turbulent flows (Ahlers, Grossmann & Lohse 2009; Lohse & Xia 2010; Chillà & Schumacher 2012; Xia 2013; Yu *et al.* 2019; Zou *et al.* 2019; Chen, Wang & Xi 2020; Wang *et al.* 2021). The main issues for thermal turbulence studies include the dynamics of turbulent structures and the scaling relation between the heat transport, in the dimensionless form, Nusselt number Nu , and thermally driven force, in the dimensionless form, Rayleigh number Ra . Recently a novel system similar to classical RBC, an annular centrifugal RBC (ACRBC) system with cold inner and hot outer cylinders corotating axially, has been proposed (Kang *et al.* 2019; Jiang *et al.* 2020; Rouhi *et al.* 2021). By exploiting strong centrifugal force through rapid rotation, the intensity of the thermal driving can be significantly enhanced.

In ACRBC, Jiang *et al.* (2020) found that the convective rolls revolve around the rotating centre in the prograde direction, signifying the emergence of zonal flow, which may be related to the effects of Coriolis force and the different curvatures of the two cylinders. In the atmospheric sciences and dynamical systems communities, a flow in the azimuthal direction is observed in the rotating cylindrical annulus, which is attributed to the baroclinic instability (Fowles & Hide 1965; Williams 1971; Read & Risch 2011; Read *et al.* 2017). The Earth's gravity and rotation both play key roles in the baroclinic waves. In astrophysical and geophysical studies, by using a rotating cylindrical annulus with conical end surfaces, Busse and his collaborators (Busse & Carrigan 1974; Azouni, Bolton & Busse 1985; Busse & Or 1986; Busse 1994) also observed a zonal flow phenomenon. According to the topographic- β approximation (Yano, Talagrand & Drossart 2005), the strength and direction of the zonal flow in their system depend on the radial gradient of the axial fluid column height. By using a spherical shell model with a radius ratio of 0.9, Heimpel, Aurnou & Wicht (2005) found that zonal flow in the equatorial latitude of Jupiter is prograde with respect to the planet, which is consistent with the actual observed results of Jupiter (Porco *et al.* 2003), but the width of equatorial zonal flow does not coincide with the predictions of Rhines scale (Rhines 1975). The physical mechanism of zonal flow in ACRBC and how it is affected by the curvatures of the two cylinders (Jiang *et al.* 2020) deserves further study.

In classical turbulent RBC, the effects of aspect ratio Γ on the Nusselt number Nu have been extensively studied (Sun *et al.* 2005; Ahlers *et al.* 2009; van der Poel, Stevens & Lohse 2011; Huang *et al.* 2013; Huang & Xia 2016) and it is found that heat transport efficiency has a great relevance on Γ when it is smaller than 1 (van der Poel *et al.* 2011). Huang *et al.* (2013) and Huang & Xia (2016) investigated the effects of lateral confinement on heat transport in quasi-two-dimensional (quasi-2-D) turbulent RBC and found that the narrow lateral width of the convection cell induces the increase of the heat transfer efficiency. In high-Reynolds number Taylor–Couette (TC) turbulence, Grossmann, Lohse & Sun (2016) analysed multiple sets of data from the previous experiments and direct numerical simulations (DNS), and found that in the range of radius ratio 0.5–0.909, as the radius ratio increases, the amplitude of TC Nusselt number Nu_ω (the dimensionless angular velocity flux) first increases, and then saturates when the radius ratio is greater than

0.7, indicating that larger radius ratio can achieve higher momentum transport efficiency. Therefore, it is of vital importance to study the effects of geometry on the heat transport efficiency of the ACRBC system, and it can also give insights for the design of rotating machinery (King, Wilson & Owen 2005; Pitz *et al.* 2017a; Chalhoun *et al.* 2018).

We notice that Pitz, Marxen & Chew (2017b) and Kang *et al.* (2019) have studied the effects of the radius ratio on the centrifugal buoyancy driven flow, but they mainly focused on the dependence of the critical Rayleigh number Ra_c and the critical wavenumber ω_c of convection onset through linear stability analysis and numerical simulation. For higher Rayleigh number Ra in the turbulent regime, to the best of our knowledge little attention has been paid to systematically studying the effects of radius ratio. To fill this gap, we present a systematic investigation of the dynamics of zonal flow and heat transfer properties in the turbulent regime of the ACRBC system with radius ratio from 0.3 to 0.9 by means of three-dimensional (3-D) DNS. Will the geometric effects in ACRBC be similar to those in RBC or in TC? Answering this question is the major objective in this study.

The remainder of this manuscript is organized as follows. In § 2, we give a brief description of the governing equations and the numerical model. The results are presented and analysed in § 3, which is divided into three parts. Section 3.1 describes the dynamics of zonal flow in ACRBC and explains the physical mechanism of it. In § 3.2, we show the dependence of heat transfer on radius ratio, and discuss the physical reasons. Remarkably asymmetric mean temperature fields are found in ACRBC and predicted by a theoretical model, which is discussed in § 3.3. Finally, we summarize our findings in § 4.

2. Numerical settings

2.1. Flow set-up

We consider a fluid bounded by cold inner and hot outer cylinders, which corotate axially as shown in figure 1. The governing equations are derived from the Navier–Stokes equations under the Boussinesq approximation in a rotating reference frame (the detailed derivation of the non-dimensional governing equations is provided in the Appendix A), which are expressed as

$$\nabla \cdot \mathbf{u} = 0, \tag{2.1}$$

$$\frac{\partial \theta}{\partial t} + \mathbf{u} \cdot \nabla \theta = \frac{1}{\sqrt{RaPr}} \nabla^2 \theta, \tag{2.2}$$

$$\frac{\partial \mathbf{u}}{\partial t} + \mathbf{u} \cdot \nabla \mathbf{u} = -\nabla p - Ro^{-1} \hat{\omega} \times \mathbf{u} + \sqrt{\frac{Pr}{Ra}} \nabla^2 \mathbf{u} - \theta \frac{2(1-\eta)}{(1+\eta)} \mathbf{r}, \tag{2.3}$$

where $\hat{\omega}$ is the unit vector pointing in the direction of the angular velocity, \mathbf{u} is the velocity vector normalized by the free-fall velocity $U \equiv \sqrt{\omega^2((R_o + R_i)/2)\alpha \Delta L}$, t is the dimensionless time normalized by L/U , and θ is the temperature normalized by Δ . Here, as defined in figure 1, ω denotes the angular velocity of the system. Here R_o and R_i are the radius of the outer and inner cylinders, respectively, α is the isobaric thermal expansion coefficient of the fluid, Δ and L are the temperature difference ($\Delta \equiv \theta_{hot} - \theta_{cold}$) and the gap ($L \equiv R_o - R_i$) between the two cylinders. In the coordinate system ϕ, z, r refer to the streamwise (azimuthal), spanwise (axial) and wall-normal (radial) directions. In the following, we will adopt $R' = (R - R_i)/(R_o - R_i)$ as the radial position to unify the cases with different η .

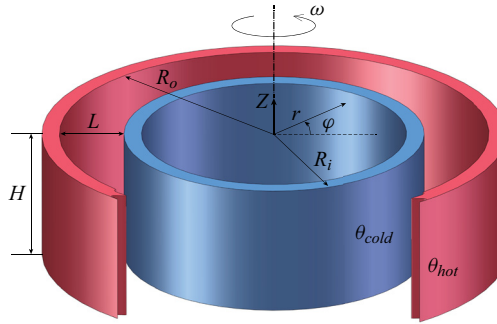


Figure 1. Schematic diagram of the flow configuration. Here ω is the angular velocity of the system. All cases in this paper set the angular velocity unit vector $\hat{\omega} = +1$, that is, the system rotates anticlockwise. Here R_o , R_i , H and L are the inner radius of the outer cylinder, the outer radius of the inner cylinder, the height of the cylindrical annulus, and the gap width between the two cylinders, respectively. Here θ_{hot} and θ_{cold} denote the temperature of the outer and inner walls.

The above dimensionless governing equations reveal that ACRBC is mainly controlled by four dimensionless parameters. Similar to classical RBC, the Rayleigh number is defined as

$$Ra = \frac{1}{2}\omega^2(R_o + R_i)\alpha\Delta L^3/(\nu\kappa), \quad (2.4)$$

and Prandtl number as $Pr = \nu/\kappa$, which characterize the buoyancy-driven strength and physical properties of the convecting fluid. Here, ν and κ are the kinematic viscosity and thermal diffusivity of the fluid, respectively. Note that the centrifugal term $-\theta(2(1 - \eta)/(1 + \eta))r$ grows linearly with the radius, which is consistent with reality. While the characteristic value of centrifugal force is $\omega^2(R_i + R_o)/2$, which is used in the definition of free-fall velocity U and Ra . Two additional control parameters are $Ro^{-1} = \omega L/U$ and $\eta = R_i/R_o$, which measure Coriolis force effects and geometric properties. The key response parameter is the Nusselt number given by

$$Nu = \frac{J}{J_{con}} = \frac{\langle u_r \theta \rangle_{\phi, z, t} - \kappa \frac{\partial}{\partial r} \langle \theta \rangle_{\phi, z, t}}{\kappa \Delta (r \cdot \ln(\eta))^{-1}}, \quad (2.5)$$

where J , J_{con} , u_r and θ denote the total heat flux, the heat flux through pure thermal conduction and the radial velocity and temperature of a certain point, respectively. Here $\langle \dots \rangle_{\phi, z, t}$ denotes taking the average over the ϕ - z -plane and time. The derivation of conductive heat flux in cylindrical geometry is slightly different from that in classical RBC, and the derivation of (2.5) is supplied in [Appendix B](#).

2.2. DNS

Numerical simulations are performed using an energy-conserving second-order finite-difference code, which has been described in detail in the literature (Verzicco & Orlandi 1996; van der Poel *et al.* 2015a; Zhu *et al.* 2018; Jiang *et al.* 2020). Thus, here we introduce it briefly and just give some main features. [Table 1](#) in [Appendix C](#) lists all the specific simulation parameters. For all cases, no-slip boundary conditions for velocity and constant temperature boundary conditions are adopted at the surfaces of the inner and outer cylinders, which is different from the free-slip boundary conditions in Goluskin *et al.* (2014), von Hardenberg *et al.* (2015) and Wang *et al.* (2020). Thus, zonal flow in

our system is much weaker and more similar to laboratory conditions. Periodic boundary conditions are imposed on \mathbf{u} and θ in the z -direction. The aspect ratio ($\Gamma = H/L$) for most cases is set $\Gamma = 1$, but for high Ra cases (i.e. $Ra > 10^7$), Γ is reduced to 0.5 and in several cases to 0.25. Furthermore, for large Ra and $0.6 \leq \eta \leq 0.9$, the azimuthal domain is reduced from a whole circle ($\phi_0 = 1$) to $\phi_0 = 1/2, 1/4, 1/8$. The flow domain at least contains a pair of convection rolls to ensure the statistical stability. It is found that such an arrangement will not have a considerable impact on Nu and zonal flow.

Adequate resolutions are ensured for all simulations and we have performed *a posteriori* checks of spatial and temporal resolutions to guarantee to resolve all relevant scales. As shown in [table 1](#), the ratio of maximum grid spacing Δ_g in the bulk region to the Kolmogorov scale estimated by the global criterion $\eta_K = LPr^{1/2}/[Ra(Nu - 1)]^{1/4} \cdot [(1 + \eta) \ln(\eta)/2(\eta - 1)]^{1/4}$ (Jiang *et al.* 2020) is smaller than 0.7 ($\Delta_g/\eta_K < 0.7$). We have also compared Δ_g with the Batchelor scale $\eta_B = \eta_K Pr^{-1/2}$ (Silano, Sreenivasan & Verzicco 2010) for each case (not shown here) and we have $\Delta_g/\eta_B < 1.4$. Furthermore, the clipped Chebychev-type clustering grids adopted in the radial direction ensure the spatial resolution within boundary layers (BLs). There are at least eight grid points inside thermal BLs and 10 grid points inside viscous BLs. We use the Courant–Friedrichs–Lewy (CFL) conditions to check temporal resolution (Courant, Friedrichs & Lewy 1928; van der Poel *et al.* 2015a; Zhang, Zhou & Sun 2017), i.e. the CFL number is smaller than 0.8 for all simulations to ensure computational stability. Here τ_{avg} is the averaging time for the Nusselt number. For simulation convergence, each case is run for approximately 100 free-fall time units to discard initial transients, and we obtain the Nu by averaging over an additional $\tau_{avg} \geq 80$ and over the Nusselt numbers at the inner (Nu_{in}) and outer (Nu_{out}) walls. One way for statistical convergence is when the difference of the Nu between inner and outer walls $\epsilon_{Nu} = |Nu_{in} - Nu_{out}|/Nu$ is small and acceptable (Ostilla *et al.* 2013; Kunnen *et al.* 2016). For most cases, ϵ_{Nu} is less than 1% and the maximum of ϵ_{Nu} is approximately 1.73%, as shown in [table 1](#).

2.3. Explored parameter space

In the present study, we aim at studying the geometric effects on ACRBC systematically. The simulations cover a radius ratio η range [0.3, 0.9] and a Ra range [$10^6, 10^8$]. Here Pr is fixed at 4.3, corresponding to the working fluids of water at 40 °C. Also, Ro^{-1} is fixed at 1, that is because when $Ro^{-1} \ll 1$, the rotation effect is too weak; while when $Ro^{-1} \gg 1$, the turbulence is suppressed, and the flow becomes quasi-2-D state. From the previous tests, we find that zonal flow is strong at $Ro^{-1} = 1$ and $Pr = 4.3$. For fixed $Ro^{-1} = 1$, the influence of rotation (Coriolis force) remains comparable for all values of the buoyancy forcing (Ra). We concentrate on the η effects on the flow structure and heat transport for different Ra while the time scales of rotation and convective motion are similar. Besides, all the results in this paper set the angular velocity unit vector $\hat{\omega} = +1$, that is, the system rotates anticlockwise.

3. Results and discussion

3.1. Zonal flow

As mentioned in Jiang *et al.* (2020), the convection rolls in ACRBC revolve in the prograde direction around the axis with a faster rotation rate than the background rotation of the experimental system, which is the so-called zonal flow. The mechanisms of zonal flow and the responses of the dynamics of zonal flow to η and Ra are discussed in § 3.1.1. Next we

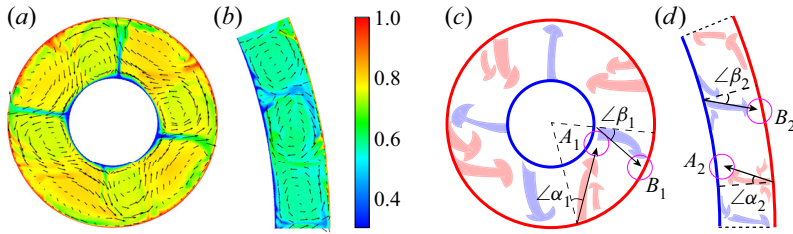


Figure 2. Typical snapshots of instantaneous temperature fields, superposed by the velocity vectors for (a) $\eta = 0.4$ and (b) $\eta = 0.9$ at $Ra = 10^7$, $Ro^{-1} = 1$ and $Pr = 4.3$. To visualize the plumes clearly, the temperature colourbar is from 0.3 to 1. (c,d) Corresponding sketches to panels (a,b), which show the motions of cold (blue) and hot (red) plumes. Here $\angle\alpha$ and $\angle\beta$ are the deflected angle of the hot and cold plumes, respectively. Here A and B are the impacting region of the hot and cold plumes, respectively. The arrows show the trajectory of the plumes.

present some statistical analyses of zonal flow, i.e. the frequency ω_d of the net rotation of the convection rolls and the strength of zonal flow $\langle u_\phi \rangle_{V,t}$ in § 3.1.2, where $\langle \cdot \cdot \rangle_{V,t}$ denotes the average over the whole volume and time.

3.1.1. Dynamics of zonal flow

Akin to the classical RBC, the direction of the temperature gradient is parallel to the centrifugal buoyancy in ACRBC. As the temperature difference or the rotation rate increases, the flow will gradually become unstable and convection appears when Ra is higher than critical Ra_c (Pitz *et al.* 2017b) of convection onset. When $Ra \gtrsim 10^6$ (Kang *et al.* 2019), the flow transitions to become turbulent in the bulk and we will focus on the turbulent convection regime.

In the rotating reference frame, the Coriolis force emerges and plays an important role. As shown in figure 2, driven by the Coriolis force, the cold and hot plumes should both have deflected to the right-hand side from the initial direction. The initial deflected angle of hot plumes ($\angle\alpha$) is roughly equal to the deflected angle of cold plumes ($\angle\beta$). As $Ro^{-1} = 1$, the Coriolis force balances inertial force and the flow is in the inertial regime. We also calculate the root-mean-square axial velocity $\langle (u_z)_{rms} \rangle_{r,\phi,z}$ for different η and Ra . It is found that $\langle (u_z)_{rms} \rangle_{r,\phi,z} \sim 0.025$ at $Ro^{-1} = 1$, which is much larger than that in the quasi-2-D state (see figure 2D of Jiang *et al.* (2020)). So the flow is still quite 3-D and not in geostrophic balance (Coriolis \sim pressure). In the inertial regime, the plumes should be deflected by the Coriolis force to roughly follow ‘inertial circles’ (Cushman-Roisin & Beckers 2011). We define the radius of the inertial circle as \widehat{R} . According to the balance relation between the inertial force and Coriolis force, $(U/\widehat{R})U \sim 2\omega U$, then the flow would deflect with a radius of curvature $\widehat{R} = U/(2\omega)$. The ejection velocity of cold plumes is larger than that of hot plumes, which would cause the radius of curvature of the trajectory circle $\widehat{R} = U/(2\omega)$ of cold plumes to be larger (see figure 2a,c). The asymmetric trajectory of plumes leads to the generation of zonal flow.

The reason for the larger ejection velocity of cold plumes is estimated from the expression of local free-fall velocity and verified from the numerical results. The local free-fall velocity $U \equiv \sqrt{(\omega^2 R)\alpha \Delta L}$. On the one hand, from the local temperature difference aspect, the temperature difference near the inner cylinder is larger than that near the outer cylinder because $\theta_m < \theta_c$ (This point will be discussed in § 3.3). On the other

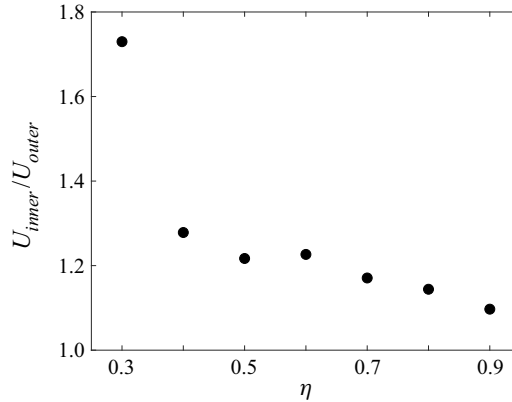


Figure 3. The ratio of local velocity for cold plumes to local velocity for hot plumes U_{inner}/U_{outer} as a function of η at $Ra = 10^7$.

hand, supergravity ($\omega^2 R$) is stronger near the outer cylinder. For example, for $\eta = 0.5$,

$$\Delta_{inner} = |\theta_{inner} - \theta_c| \sim 0.75\Delta, \quad \Delta_{outer} = |\theta_{outer} - \theta_c| \sim 0.25\Delta, \quad (3.1a,b)$$

$$\frac{U_{inner}}{U_{outer}} = \frac{\sqrt{(\omega^2 R_{inner})\alpha \Delta_{inner} L}}{\sqrt{(\omega^2 R_{outer})\alpha \Delta_{outer} L}} \sim \sqrt{\frac{3}{2}} \approx 1.22. \quad (3.2)$$

Therefore, the deflection angle of the cold plumes at the inner boundary is smaller because the local radius of curvature $\hat{R} = U/2\omega$ is larger. Further, we compare the radial velocity $|u_r|$ of the cold plumes and hot plumes. Because the strength of zonal flow is relatively strong at $Ra = 10^7$, we study the radial velocity $|u_r|$ versus η at $Ra = 10^7$. According to the azimuthal distribution of the radially and axially averaged radial velocity $\langle u_r \rangle_{r,z}$, we can detect the positions of the cold and hot plumes. The velocities of plumes are then averaged by time (20 free-fall time units, 0.2 time interval) and each roll. As shown in figure 3, cold plumes have a larger local velocity than hot plumes. The ratio of local velocity for cold plumes $|u_{r,c}| = U_{inner}$ to local velocity for hot plumes $|u_{r,h}| = U_{outer}$ decreases with η increasing, which is consistent with the trend of zonal flow strength versus η (discussed in § 3.1.2).

Next, we provide the second mechanism of the generation of zonal flow. Because of the different curvatures of the inner and outer cylinders (see figure 2a,c, $\eta = 0.4$), the hot plumes deflect and then impact on A_1 , which is close to the region where the cold plumes are ejected, whereas the distance between the impacting region B_1 of the cold plumes and the emitting region of hot plumes is relatively large. Consequently, the hot plumes ‘win’ and push the overall flow to move anticlockwise. Some cold plumes even deflect to the left-hand side due to the impact of hot plumes. For comparison, the difference between the curvatures of the hot and cold walls is small at $\eta = 0.9$ (see figure 2b,d) and both the impacting regions A_2 and B_2 are far away from the ejecting positions of cold and hot plumes, respectively. Thus, zonal flow becomes weaker with η increasing. Note that this mechanism of the zonal flow is different from the ‘inertial circle’ theory. Even though the radius of curvature of the trajectories of cold and hot plumes are the same, plume impingement will also occur. Figure 4(a–c) shows the instantaneous temperature fields for different radius ratios η at $Ra = 10^7$. When $\eta = 0.3$ (figure 4a, also see supplementary movie 1 available at <https://doi.org/10.1017/jfm.2021.889>), the deflected distances of hot plumes are remarkably larger than the cold plumes. When $\eta = 0.6$ (figure 4b, also see

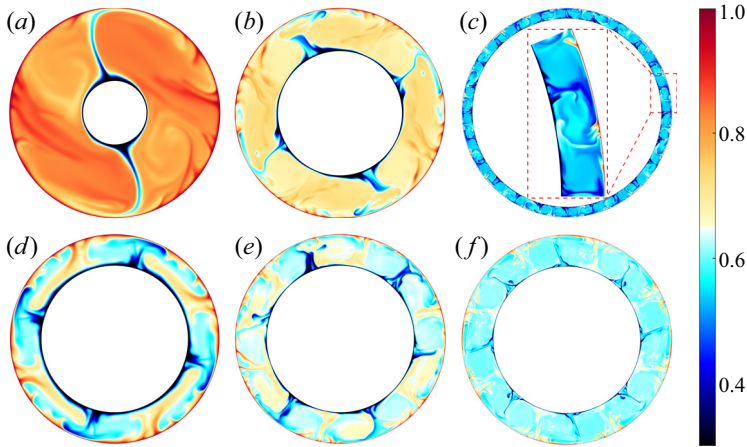


Figure 4. (a–c) Instantaneous temperature fields on a ϕr -plane for $\eta = 0.3, 0.6, 0.9$ at $Ra = 10^7$, $Ro^{-1} = 1$ and $Pr = 4.3$. (d–f) Instantaneous temperature fields for $Ra = 10^6, 10^7, 10^8$ at $\eta = 0.7$, $Ro^{-1} = 1$ and $Pr = 4.3$. To visualize the plumes clearly, the temperature colourbar is from 0.3 to 1. All figures share the same colourbar.

supplementary movie 2), the asymmetric movements of cold and hot plumes still could not be ignored. Hot plumes can impact on the root region of the cold plumes, but on the contrary the impacting region of cold plumes cannot affect the hot plumes directly. When $\eta = 0.9$ (figure 4c, also see supplementary movie 3), the movements of cold and hot plumes are almost symmetric, and there are several pairs of LSC rolls without distinct azimuthal movement, which is similar to the classical RBC.

Figure 4(d–f) demonstrates the influences of Ra on flow structures for $\eta = 0.7$. As we know, for classical RBC the aspect ratio of convection rolls is approximately equal to one without the confinement effects of sidewalls, which is almost consistent with the case of $Ra = 10^8$ in ACRBC (see figure 4f). However, we find that the wavenumber decreases with the decrease of Ra . This is because with the increase of Ra , the flow is more turbulent and the thermal BLs become more unstable. There are more thermal plumes detaching from the BLs and more convection rolls are formed. As shown in figure 5, it is indicated that the number of roll pairs N is smaller than the circular roll hypothesis (Pitz *et al.* 2017b), $\eta = (2N - \pi)/(2N + \pi)$, for almost all cases. The convection rolls are probably elongated by strong zonal flow. At $Ra = 10^6$ or small η , N is much smaller than the theoretical line, which is consistent with the strong zonal flow in this Ra and η regime.

3.1.2. Quantitative analysis of zonal flow

Figure 6(a–c) give the azimuth-time temperature contours at the midradius and midheight position for $\eta = 0.3, 0.6$ and 0.9 , respectively, which show that the convection rolls revolve in the prograde direction. And besides, the convection rolls drift at a nearly constant rate with high frequency oscillations. Similar effects have also been reported in Pitz *et al.* (2017b). Figure 6(d) suggests that the drift frequency ω_d decreases with η increasing (averaged over 100 free-fall time units), where ω_d is defined as the azimuthal movement (radians) of convection rolls per free-fall time unit in the rotating frame. It is found that $\omega_d = -0.05\eta + 0.05$ for $0.7 \leq \eta \leq 0.9$, while it gives a notably steeper slope with $\omega_d = -0.2\eta + 0.15$ for $0.3 \leq \eta \leq 0.7$. This change of the slope of ω_d versus η indicates that the influence of curvature effects on the drift frequency of convection rolls is more significant at small η .

Effects of radius ratio on annular centrifugal convection

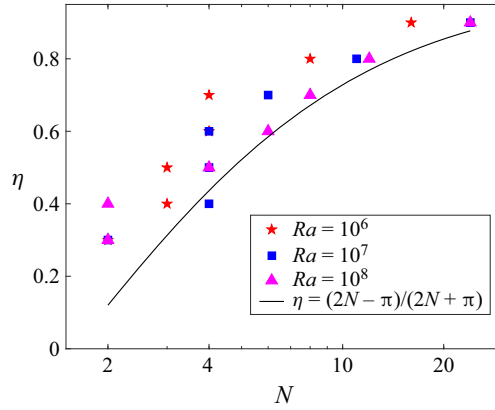


Figure 5. Radius ratio η as a function of the number of roll pairs N for different Ra . The solid line is the circular roll hypothesis as zonal flow is weak.

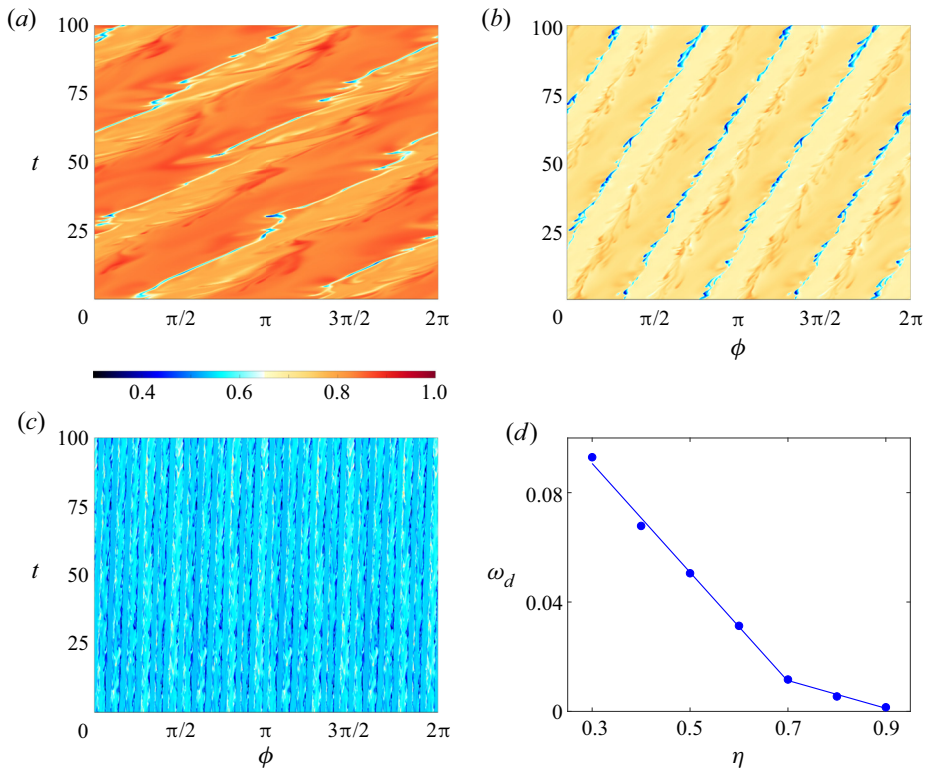


Figure 6. Azimuth-time temperature contours at the midradius and midaxial position for (a) $\eta = 0.3$, (b) $\eta = 0.6$ and (c) $\eta = 0.9$ at $Ra = 10^7$. To visualize the plumes clearly, the temperature colourbar is from 0.3 to 1. All temperature fields share the same colourbar. (d) Drift frequency ω_d of the convection rolls versus η at $Ra = 10^7$, where ω_d is the drift angle (radians) per dimensionless time t . The solid lines are the best linear fits of $\omega_d(\eta)$ for $0.3 \leq \eta \leq 0.7$ and $0.7 \leq \eta \leq 0.9$, respectively.

Since that when there are no systematic deflections of plumes, one would expect that $\langle u_\phi \rangle_{\phi,z,t}$ vanishes. Now $\langle u_\phi \rangle_{\phi,z,t}$ can reflect the asymmetric extent of the motion of cold and hot plumes. As shown in figure 7(a), with the decrease of η , the positive $\langle u_\phi \rangle_{\phi,z,t}$ (reflects the deflection of hot plumes) is larger and the negative part (reflects the deflection

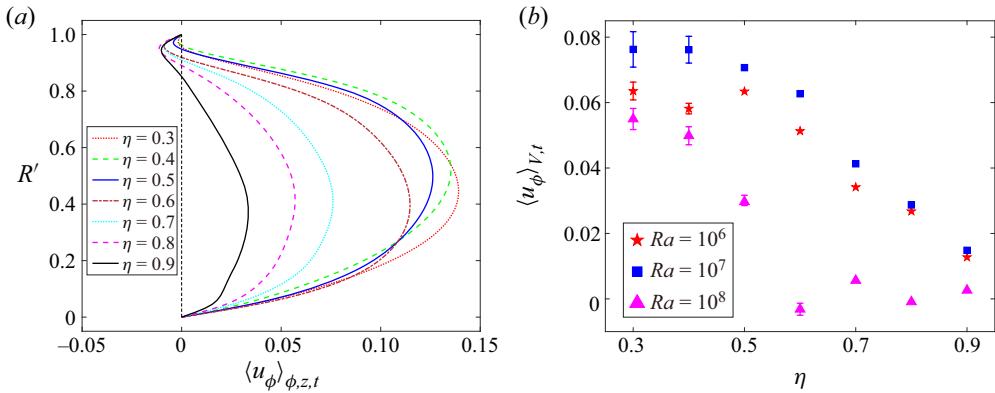


Figure 7. (a) Azimuthal velocity profiles averaged azimuthally, axially and by time along the radial direction $R' = (R - R_i)/(R_o - R_i)$ for different η at $Ra = 10^7$. (b) Mean azimuthal velocity $\langle u_\phi \rangle_{V,t}$ as a function of η for different Ra . Error bars are the standard deviations of the time series of $\langle u_\phi \rangle_V$. If the error bar is not visible, it is smaller than the symbol size.

of cold plumes) is smaller in absolute value. We calculate the Reynolds stress $\langle u'_\phi u'_r \rangle_{\phi,z,t}$ and find that the Reynolds stress is negative along the radius, which possibly results from the tilted plumes. Negative ϕ -momentum is transported in the positive r -direction and positive ϕ -momentum is transported in negative r -direction. Thus a strong prograde zonal flow develops in the inner part of the annulus. Figure 7(b) shows that, basically, for each fixed Ra , space- and time-averaged azimuthal velocity all decrease as η increases. Thus, the drift of LSC rolls is directly linked to the asymmetric motion of cold and hot plumes. In addition, we find that at moderate Ra ($Ra = 10^7$), zonal flow is the strongest. When $Ra = 10^6$, the velocity of plumes is slow due to the weak buoyancy (relative to viscosity); while when $Ra = 10^8$, the flow is more turbulent and the coherent length of plumes decreases. So the zonal flow driven by the plumes for both cases is relatively weak. We also note that when $\eta \lesssim 0.5$ for $Ra = 10^6$ and 10^7 or $\eta \lesssim 0.4$ for $Ra = 10^8$ (figure 7b), $\langle u_\phi \rangle_{V,t}$ no longer increases remarkably as η decreases, which is probably a consequence of the increase of the gap width of the convection cell. The long distance to reach the opposite surfaces results in the reduction of the strength of plumes, and $\langle u_\phi \rangle_{V,t}$ reaches saturation.

3.2. Heat transport

Figure 8(a) shows Nu as a function of Ra for $0.3 \leq \eta \leq 0.9$. When $\eta = 0.3$ or 0.4 , $Nu(Ra)$ can be described with a power law $Nu \sim Ra^\gamma$ with a scaling exponent γ of 0.28 ± 0.01 (see figure 8b). With the increase of η , γ gradually increases to 0.33 ± 0.02 at $\eta \sim 0.7$ and slightly decreases for larger η . The inset of figure 8(a) shows $NuRa^{-0.32}$ as a function of Ra , also suggesting that when $\eta = 0.3$, γ is relatively small. In TC turbulence, the dimensionless angular velocity flux Nu_ω also increases as η increases, reaches saturation when $\eta \gtrsim 0.7$ and slightly decreases for larger η (Grossmann *et al.* 2016). So for flow in a rotating cylindrical annulus system, there may exist a unified law that transport efficiency is higher in the system with larger η . In figure 9(a), we plot the normalized Nu (normalized by Nu at $\eta = 0.9$ for the respective Ra) as a function of η . It is clearly seen that Nu decreases with the decrease of η for each Ra . For the case of $Ra = 10^8$ and $\eta = 0.3$, Nu is only approximately 70% of that at $\eta = 0.9$. What is the physical reason for the η dependence of heat transport?

Effects of radius ratio on annular centrifugal convection

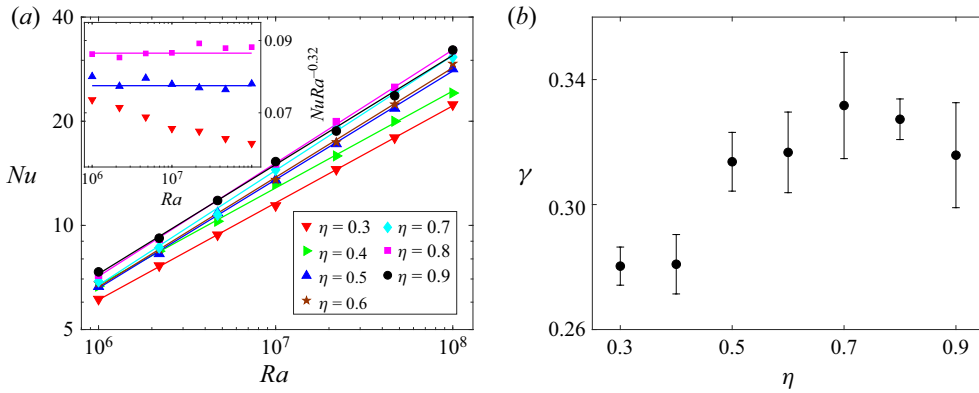


Figure 8. (a) Nusselt number Nu as a function of Rayleigh number Ra for different η . The inset shows $NuRa^{-0.32} \sim Ra$ for $\eta = 0.3, 0.5, 0.8$. (b) Scaling exponents γ obtained by fitting $Nu \sim Ra^\gamma$ as a function of η . Error bar is the range of fitting exponent within 95 % confidence interval.

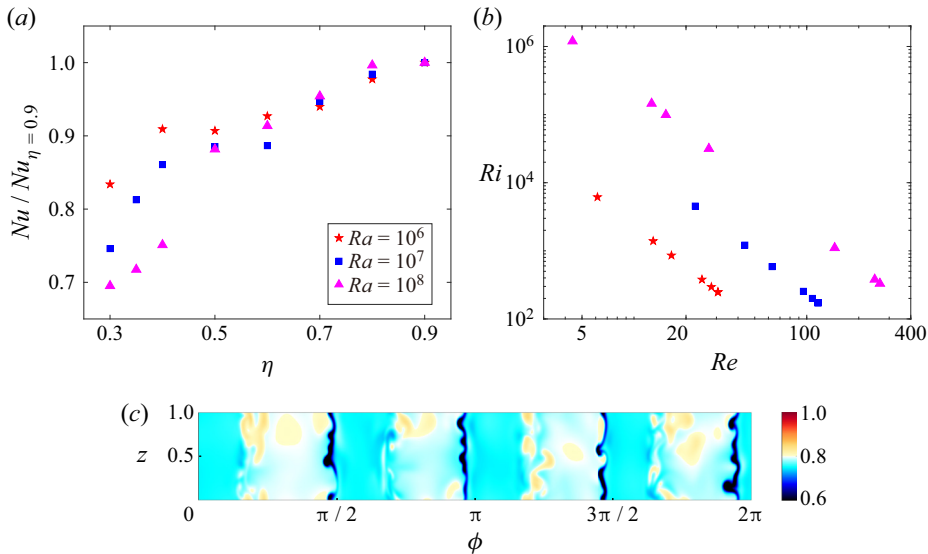


Figure 9. (a) Plot of $Nu/Nu_{\eta=0.9}$ as a function of η for different Ra . Here $Nu/Nu_{\eta=0.9}$ denotes Nusselt number normalized by the value at $\eta = 0.9$ for the respective Ra . (b) Plot of Ri versus Re for different Ra and $\eta = 0.3 \sim 0.9$. (c) Instantaneous snapshots of temperature field at midradius position for $Ra = 10^7$ and $\eta = 0.4$. To visualize the flow structure at midradius position clearly, the temperature colourbar is from 0.6 to 1.

As mentioned in § 3.1, the decrease of η results in stronger zonal flow. One possible reason is that thermal plumes are swept away by the shear of zonal flow. Thus, the heat transport is depressed. We adopt the bulk Richardson number $Ri = Ra/(Re^2Pr)$ to investigate the competition between the buoyancy and shear effects, where the Reynolds number $Re = \langle u_\phi \rangle_{V,t} L/\nu$ reflects the effect of the zonal flow shear. As shown in figure 9(b), it is found that the minimum Ri is 171.9 corresponding to $Ra = 10^7$ and $\eta = 0.3$. From the ϕz temperature field at the midradius position (see figure 9c), it is found that the main flow structure resembles the bulk flow found in RB convection.

Note that elongated streaks along the shear flow do not exist for this case with the maximum shear effects, which suggests that the flow is dominated by the buoyancy for all cases. Recently, Blass *et al.* (2020) have added shearing effects to classical RBC by pulling the top and bottom plates in opposite directions, i.e. the so-called Couette–RB flow. According to the behaviour of the flow structures versus Ri and Re , they considered that the flow states are divided into three regimes: the buoyancy dominated regime; transitional regime; shear dominated regime. In ACRBC, Ri is larger than the order of $O(100)$ and Re is no more than 300. So the flow is in the buoyancy dominated regime. From figure 5(b) of the paper of Blass *et al.* (2020), we can estimate that the reduction of Nu is only approximately 3% for $Re = 300$ at $Ra = 10^8$ by linear interpolation. Thus, the relatively weak shear effect of zonal flow can inhibit heat transfer, but the effect is very weak. It is considered that the decrease of heat transport for small η may be due to the geometric confinement effects primarily, which needs to be further studied. Goluskin *et al.* (2014) found the reduction of heat transport by the sustained versions of shearing convection. Note that they adopted the free-slip boundary condition so zonal flow is much stronger. Different Pr may also be a reason for different effects of zonal flow on Nu .

We also investigate the effects of radius ratio on the heat transport from the perspective of plumes. Employing the method introduced in Huang *et al.* (2013), van der Poel *et al.* (2015b), Chong *et al.* (2017) and Jiang *et al.* (2018), the cold plume coverage at the edge of the thermal BL of the outer cylinder is obtained. Figure 10(a,b) displays the temperature field near the outer surface for $\eta = 0.4$ and 0.9, respectively. It is evident that when $\eta = 0.9$, the area of cold plumes is larger. Figure 10(c) shows the ensemble-averaged portion of area $A_{pl}/(L_\phi L_z)$ covered by the cold plumes in the vicinity of the outer surface. As η decreases, a smaller portion of cold plumes can travel to the opposing BL. Consequently, temperature fluctuations of the thermal BL of the outer surface are smaller (see figure 10d) and the heat transfer efficiency declines.

3.3. Asymmetric mean temperature fields

In classical RBC, due to the Oberbeck–Boussinesq (OB) approximation (Oberbeck 1879), it is generally assumed that the fluid properties are constant, except for the linear variation of the density with temperature in the buoyancy term. However, when the temperature difference Δ between the hot and cold walls is large enough, the drastic changing of fluid properties should be taken into consideration. In this situation, the top–bottom symmetry of the system is broken and the bulk temperature θ_c deviates from the arithmetic mean temperature of hot and cold walls θ_m , which are known as non-OB (known as NOB) effects (Wu & Libchaber 1991; Yik, Valori & Weiss 2020).

Although we implement OB approximation in the numerical simulations of ACRBC, remarkable deviation of θ_c from θ_m is observed, which is similar to the non-OB effects. Figure 11(a) shows the radial temperature profiles averaged azimuthally, axially and over time. It is evident that θ_c is much larger than θ_m . With η increasing, the deviation $(\theta_c - \theta_m)/\Delta$ decreases for each Ra (see figure 11b), which illustrates that the mean temperature profile gradually behaves similarly to the classical RBC. We also perform some experiments in the ACRBC system. Details about the experimental set-up are introduced in Jiang *et al.* (2020). A small thermistor (Measurement Specialties, GAG22K7MCD419, with a response time of 30 ms in liquids) is inserted into the bulk flow to measure θ_c . Another type of thermistor (Omega, 44 131), evenly distributed along the circumferential direction in the cylinders, are used to obtain θ_m . Now $(\theta_c - \theta_m)/\Delta$ at $\eta = 0.5$ for experiments are slightly larger than the cases of DNS, which probably

Effects of radius ratio on annular centrifugal convection

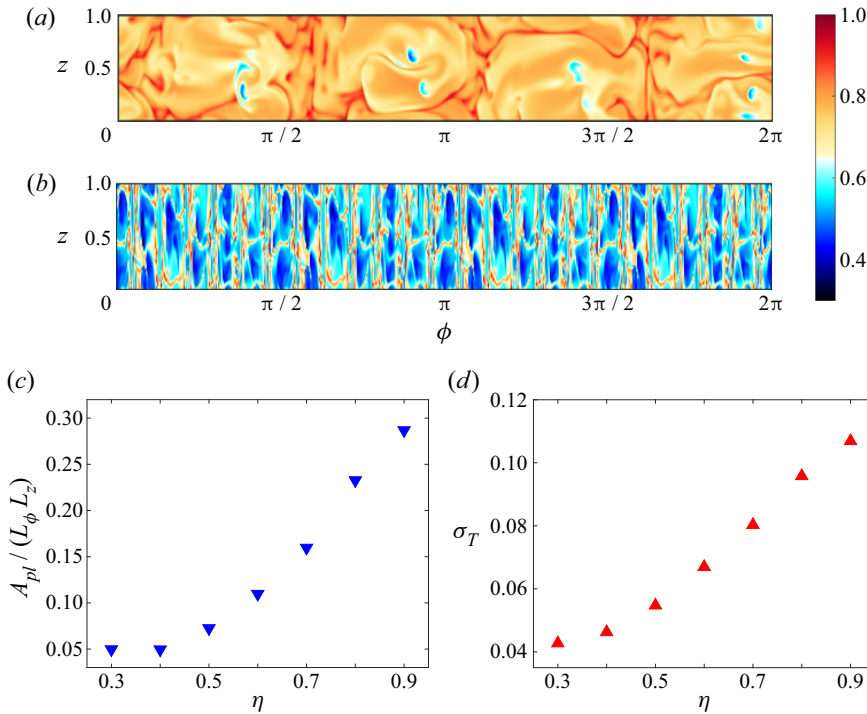


Figure 10. (a) Instantaneous temperature fields in ϕz -plane at the edge of the thermal BL ($r_s = R_o - \delta_T$) for (a) $\eta = 0.4$, (b) 0.9 at $Ra = 10^7$, where δ_T is the thickness of thermal BL obtained using the slope method (Gastine, Wicht & Aurnou 2015). To visualize the plumes clearly, the temperature colourbar is from 0.3 to 1. Panels (a,b) share the same colourbar. (c) Ensemble-averaged area of cold plumes normalized by the total area versus η . (d) Ensemble-averaged standard deviation of temperature at the position of r_s versus η .

results from the relatively large Ra and Ro^{-1} for experiments ($Ra = 6 \times 10^{10}$, $Pr = 4.3$ and $Ro^{-1} = 18$).

Next, we provide a theoretical explanation for the increase of the deviation $(\theta_c - \theta_m)/\Delta$ with η decreasing. Since the area of the outer cylinder is larger than that of the inner cylinder, according to Fourier’s law, the temperature gradient near the outer wall is smaller. Therefore, the temperature at the midradius position for pure thermal conduction state $(\theta_c)_{cond} = -(1/\ln \eta) \ln[1/2 + 1/(2\eta)]$ (derived in Appendix B) is slightly higher than $\theta_m = 0.5$. Also $(\theta_c)_{cond} - \theta_m$ as a function of η is indicated by the solid line in figure 11(b). While the curvature effect of ACRBC accounts for a part of $(\theta_c - \theta_m)/\Delta$, the difference from the total deviation is still finite. To analytically access $(\theta_c - \theta_m)/\Delta$ observed in DNS and experiments, we first assume that heat is purely transported by conduction in the thin thermal BLs. According to the conservation of heat flux through cylindrical surfaces,

$$\eta \frac{\Delta\theta^i}{\lambda^i} = \frac{\Delta\theta^o}{\lambda^o}, \quad (3.3)$$

where the thermal BL near the inner (outer) wall is assumed to be a conduction profile with a temperature difference $\Delta\theta^i$ ($\Delta\theta^o$) over a thickness λ^i (λ^o). Note that different curvatures of the two cylinders are considered in this assumption. As shown in figure 11(a), the bulk fluid is basically isothermal (for small η , the slight overshoot of temperature near the outer surface may result from the effect of Coriolis effects). Thus, we can further assume that

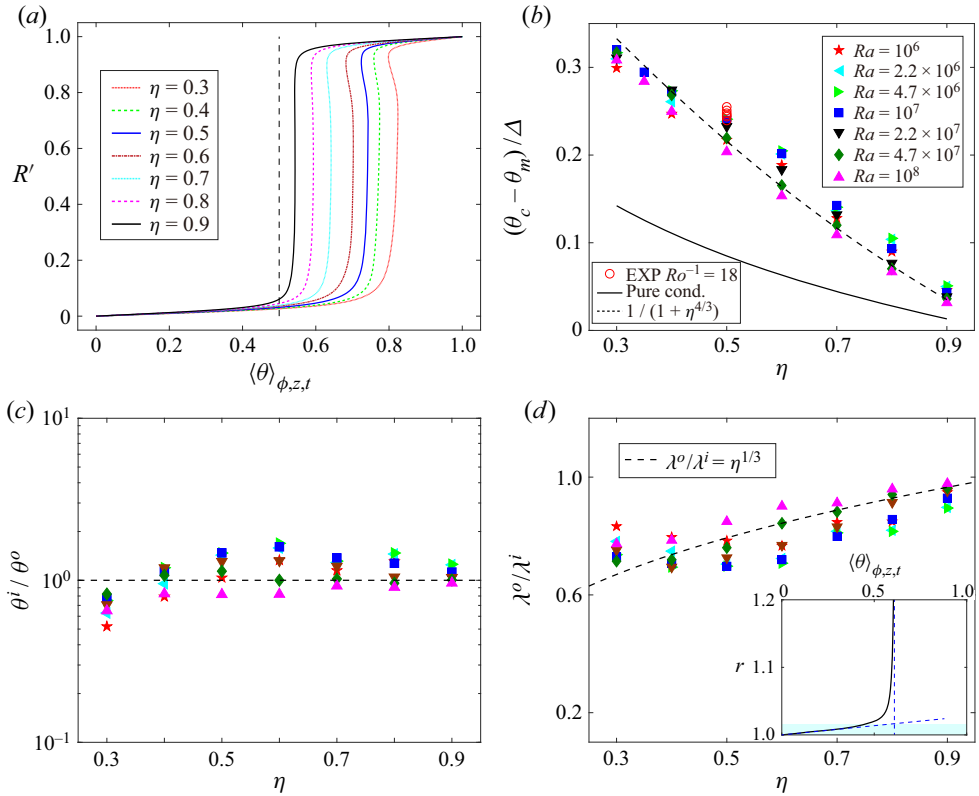


Figure 11. (a) Azimuthally, axially and time-averaged radial temperature profiles for different η at $Ra = 10^7$. (b) Relative deviation of the bulk temperature (θ_c) from arithmetic mean temperature (θ_m) of the two cylinders ($\theta_c - \theta_m$)/ Δ versus η for different Ra from DNS (the solid symbols), experiments (the open symbols) and the theoretical prediction given in (3.6) (dashed line). The experiments are performed at $\eta = 0.5$, $Ra = 6 \times 10^{10}$, $Pr = 4.3$ and $Ro^{-1} = 18$. The solid line denotes ($\theta_c - \theta_m$)/ Δ in pure thermal conduction state for comparison. (c) Ratio of BL temperature scales θ^i/θ^o versus η for different Ra . The horizontal dashed line corresponds to the hypothetical identity $\theta^i = \theta^o$ (see (3.5)). (d) Ratio of thermal BL thicknesses. The dashed line corresponds to the theoretical prediction given in (3.8). The inset of panel (d) shows the inner thermal BLs λ^i highlighted by the blue shaded area. $\lambda^{i,o}$ are defined as the distances where the tangents of the temperature profiles at the plate cross $\langle \theta \rangle_{\phi,z,t} = \theta_c$.

the temperature drops occur only in the BLs:

$$\Delta\theta^i + \Delta\theta^o = 1. \tag{3.4}$$

Equations (3.3) and (3.4) are not sufficient to determine the three unknowns $\Delta\theta^i$, $\Delta\theta^o$ and λ^i/λ^o . So an additional physical assumption is required.

Wu & Libchaber (1991), Zhang, Childress & Libchaber (1997) and Gastine *et al.* (2015) proposed that the thermal BLs adjust their length scales so that the mean hot and cold temperature fluctuations are equal in the bulk region. Temperature fluctuations in the bulk region are caused by plumes detaching from the BLs. So this implies the equality of the temperature scales for the two BLs ($\theta^{i,o} \equiv (\nu\kappa)/(\alpha g_{i,o}(\lambda^{i,o})^3)$). This third assumption yields

$$\theta^i = \theta^o \rightarrow \frac{\nu\kappa}{\alpha g_i(\lambda^i)^3} = \frac{\nu\kappa}{\alpha g_o(\lambda^o)^3}, \tag{3.5}$$

where the centrifugal acceleration $g = \omega^2 r$, so $\chi_g = g(R_i)/g(R_o) = \eta$ reflects radially dependent gravity effects. Figure 11(c) shows θ^i/θ^o for different η and Ra . Compared with turbulent RB convection in spherical shells reported by Gastine *et al.* (2015) (see their figure 5a), the identity of the BL temperature scale is better fulfilled in ACRBC. The temperature drops at both boundaries and the ratio of the thermal BL thicknesses can then be derived using (3.3)–(3.5) as

$$\Delta\theta^i \simeq \theta_c = \frac{1}{1 + \chi_g^{1/3}\eta} = \frac{1}{1 + \eta^{4/3}}, \quad (3.6)$$

$$\Delta\theta^o = \frac{1}{1 + \eta^{-4/3}}, \quad (3.7)$$

$$\lambda^o/\lambda^i = \eta^{1/3}. \quad (3.8)$$

Figure 11(b) shows that the predicted value (3.6) and the actual values for mean bulk temperature are in good agreement. We adopt the slope method to define the thickness of thermal BL λ as the distance where the tangent of the temperature profiles at the plate intersects $\langle\theta\rangle_{\phi,z,t} = \theta_c$ (see the inset of figure 11d). Figure 11(d) shows that the theory (3.8) can also predict the asymmetry of the thermal BLs λ^o/λ^i . In a word, the theory accurately accounts for the bulk temperature and the BL asymmetry for different η observed in ACRBC. The asymmetry is likely caused by the curvature effects (3.3) and radially dependent centrifugal force (3.5). We note that, although asymmetric mean temperature fields exist in ACRBC, their influence on global heat transport has been shown to be negligible (Jiang *et al.* 2020).

4. Conclusion

We present an analysis of the zonal flow, heat transport and asymmetric mean temperature field in ACRBC, by means of 3-D DNS and some experiments, with radius ratio η varying from 0.3 to 0.9, Ra varying from 10^6 to 10^8 and Pr, Ro^{-1} fixed at 4.3 and 1, respectively. Major findings are summarized as follows.

Firstly, convection rolls move anticlockwise around the axis with a faster rotation rate than the background rotation of ACRBC system (zonal flow). We provide two mechanisms for the generation of zonal flow. (1) As the flow is in the inertial regime, the plumes deflect with a radius of curvature $\hat{R} = U/(2\omega)$. The ejection velocity of the cold plumes is larger than that of hot plumes. Thus, the local curvature of the cold plume path is smaller and zonal flow is prograde pushed by the large deflection of hot plumes. (2) Due to the different curvatures of the inner and outer cylinders, the hot plumes can directly affect the ejecting position of the cold plumes, while the impact of the cold plumes does not directly affect the hot plumes. The asymmetric motions of cold and hot plumes push the overall flow to move in the same direction as the background rotation. The mechanism of zonal flow is verified by the variation of the flow behaviour with radius ratio. We observe that the drift frequency decreases with η increasing. It is also found that $\langle u_\phi \rangle_{v,t}$ decreases as η increases for each Ra . In addition, zonal flow is the strongest at moderate Ra ($Ra = 10^7$), which suggests zonal flow is related to the buoyancy and flow strength.

Secondly, the scaling exponent γ of $Nu(Ra)$ increases with η for $\eta \lesssim 0.7$ and slightly decreases for larger η . The dependence of transport efficiency on η is similar to TC flow. Furthermore, $Nu/Nu_{\eta=0.9}$ decreases with the decrease of η for each Ra . By analysing the flow field and the ratio of buoyancy and shear effects, it is found that the flow is in

the buoyancy dominated regime and the influence of shear effects of zonal flow on heat transfer is not strong in the parameter space of the current study. Additionally, we observed that the cold plume coverage at the edge of the thermal BL of the outer cylinder becomes smaller as η decreases.

Thirdly, the bulk temperature θ_c is found to be much higher than θ_m (0.5) by DNS and experiments. The relative deviation $(\theta_c - \theta_m)/\Delta$ increases with the decrease of η for each Ra . The results of numerical simulations and experiments are consistent, even though the values of Ra and Ro^{-1} are distinct. By assuming pure conduction in the thermal BLs, isothermal bulk fluid, and the equality of the temperature scales for the two boundary layers, we analytically obtain the mean bulk temperature and the ratio of the thickness of the BLs, which are in good agreement with the actual values. The asymmetric mean temperature fields may result from curvature effects and the radially dependent centrifugal force involved in the hypotheses of the theory.

In the laboratory experiment, centrifugal buoyancy can be larger than the Earth's gravity through the rapid rotation of ACRBC. Hypergravitational thermal convection is a new method to achieve high Ra (Jiang *et al.* 2020). Systematic study on the dependence of turbulent flow structures and heat transport on radius ratio is urgently needed to understand the flow dynamics in ACRBC. The physical mechanism of zonal flow may improve understanding of some flow phenomena in astrophysical and geophysical settings. Furthermore, the bulk temperature can be significantly increased in the hypergravitational thermal convection system by reducing η , which give insights for the flow and temperature control in engineering applications.

Supplementary movies. Supplementary movies are available at <https://doi.org/10.1017/jfm.2021.889>.

Funding. This work was supported by the Natural Science Foundation of China (grant nos. 11988102, 91852202, 11861131005) and Tsinghua University Initiative Scientific Research Program (grant no. 20193080058).

Declaration of interests. The authors report no conflict of interest.

Author ORCID.

- ① Dongpu Wang <https://orcid.org/0000-0002-1421-2210>;
- ① Hechuan Jiang <https://orcid.org/0000-0003-3069-0586>;
- ① Shuang Liu <https://orcid.org/0000-0002-1476-4082>;
- ① Xiaojuan Zhu <https://orcid.org/0000-0002-7878-0655>;
- ① Chao Sun <https://orcid.org/0000-0002-0930-6343>.

Appendix A. Derivation of the governing equations

Below we provide the detailed derivation of the non-dimensional governing equations. Firstly, for ACRBC the fluid motion in the rotating reference frame is governed by the continuity equation, the thermal advection–diffusion equation and the Navier–Stokes equation with centrifugal force and Coriolis force, which read

$$\nabla \cdot \mathbf{u} = 0, \tag{A1}$$

$$\frac{\partial T}{\partial t} + (\mathbf{u} \cdot \nabla)T = \kappa \nabla^2 T, \tag{A2}$$

$$\frac{\partial \mathbf{u}}{\partial t} + (\mathbf{u} \cdot \nabla)\mathbf{u} = -\frac{1}{\rho} \nabla p - 2\boldsymbol{\omega} \times \mathbf{u} + \nu \nabla^2 \mathbf{u} - \boldsymbol{\omega} \times (\boldsymbol{\omega} \times \mathbf{r}). \tag{A3}$$

Here \mathbf{u} , t , T and p are the velocity, time, temperature and pressure of the flow; ρ , ν , κ are the density, kinematic viscosity, thermal diffusivity of the working fluid, respectively; $\boldsymbol{\omega}$ is the angular velocity of the system. Different from Navier–Stokes equation in the inertial frame, two additional terms appear and they are the Coriolis force $-2\boldsymbol{\omega} \times \mathbf{u}$ and the centrifugal force $-\boldsymbol{\omega} \times (\boldsymbol{\omega} \times \mathbf{r})$.

Secondly, spatially and temporally constant temperatures are assumed at the hot and cold surfaces. The problem is simplified by the OB approximation in which the fluid density ρ is assumed to depend linearly on the temperature only in the centrifugal buoyancy term,

$$\rho(T) = \rho(T_0)[1 - \alpha(T - T_0)], \tag{A4}$$

where T_0 is the reference temperature at the inner cylinder. Here α is the thermal expansion coefficient of the working fluid. Substituting (A4) into (A3), the governing equations are

$$\nabla \cdot \mathbf{u} = 0, \tag{A5}$$

$$\frac{\partial T}{\partial t} + (\mathbf{u} \cdot \nabla)T = \kappa \nabla^2 T, \tag{A6}$$

$$\frac{\partial \mathbf{u}}{\partial t} + (\mathbf{u} \cdot \nabla)\mathbf{u} = -\frac{1}{\rho} \nabla p - 2\boldsymbol{\omega} \times \mathbf{u} + \nu \nabla^2 \mathbf{u} - \alpha \delta T \boldsymbol{\omega}^2 \mathbf{r}. \tag{A7}$$

Here, $\delta T = T - T_0$ is the temperature difference from the reference temperature.

Thirdly, we non-dimensionalize the set of equations using the gap width L , the free-fall velocity $U \equiv \sqrt{\omega^2((R_o + R_i)/2)\alpha \Delta L}$ (R_o and R_i are the radius of the outer and inner cylinders, respectively) and the temperature difference of the inner and outer cylinders Δ . Then we arrive at the dimensionless governing equations as follows:

$$\tilde{\nabla} \cdot \tilde{\mathbf{u}} = 0, \tag{A8}$$

$$\frac{\partial \tilde{\theta}}{\partial \tilde{t}} + \tilde{\mathbf{u}} \cdot \tilde{\nabla} \tilde{\theta} = \frac{\kappa}{\omega L \sqrt{(R_o + R_i)\alpha \Delta L/2}} \tilde{\nabla}^2 \tilde{\theta}, \tag{A9}$$

$$\begin{aligned} \frac{\partial \tilde{\mathbf{u}}}{\partial \tilde{t}} + \tilde{\mathbf{u}} \cdot \tilde{\nabla} \tilde{\mathbf{u}} = & -\tilde{\nabla} \tilde{p} - 2 \left(\frac{\alpha \Delta (R_o + R_i)}{2L} \right)^{-1/2} \hat{\boldsymbol{\omega}} \times \tilde{\mathbf{u}} \\ & + \frac{\nu}{\omega L \sqrt{(R_o + R_i)\alpha \Delta L/2}} \tilde{\nabla}^2 \tilde{\mathbf{u}} - \tilde{\theta} \frac{2L}{R_i + R_o} \tilde{\mathbf{r}}, \end{aligned} \tag{A10}$$

where $\tilde{r} = r/L$ and $\tilde{t} = tU/L$ are the scaled space and time coordinates; $\tilde{\mathbf{u}} = \mathbf{u}/U$, $\tilde{p} = (p - \rho(T_0)\omega^2 R_i^2/2)/(\rho(T_0)U^2)$; $\tilde{\theta} = (T - T_0)/\Delta$ are the scaled velocity, the scaled pressure and temperature variation, respectively; $\hat{\boldsymbol{\omega}}$ is the unit vector pointing in the direction of the angular velocity.

Lastly, four dimensionless parameters will be deduced in the governing equations:

$$\eta = R_i/R_o, \tag{A11}$$

$$Ra = \frac{1}{2} \omega^2 (R_o + R_i) \alpha \Delta L^3 / (\nu \kappa), \tag{A12}$$

$$Pr = \nu/\kappa, \tag{A13}$$

$$Ro^{-1} = 2\omega L/U = 2(\alpha \Delta (R_o + R_i)/(2L))^{-1/2}. \tag{A14}$$

Substituting these control parameters (A11)–(A14) into (A8)–(A10), we obtain

$$\tilde{\nabla} \cdot \tilde{\mathbf{u}} = 0, \tag{A15}$$

$$\frac{\partial \tilde{\theta}}{\partial \tilde{t}} + \tilde{\mathbf{u}} \cdot \tilde{\nabla} \tilde{\theta} = \frac{1}{\sqrt{RaPr}} \tilde{\nabla}^2 \tilde{\theta}, \tag{A16}$$

$$\frac{\partial \tilde{\mathbf{u}}}{\partial \tilde{t}} + \tilde{\mathbf{u}} \cdot \tilde{\nabla} \tilde{\mathbf{u}} = -\tilde{\nabla} \tilde{p} - Ro^{-1} \hat{\boldsymbol{\omega}} \times \tilde{\mathbf{u}} + \sqrt{\frac{Pr}{Ra}} \tilde{\nabla}^2 \tilde{\mathbf{u}} - \tilde{\theta} \frac{2(1-\eta)}{(1+\eta)} \tilde{\mathbf{r}}. \tag{A17}$$

For clarity, the wave line cap $\tilde{\cdot}$ for the dimensionless quantity is omitted. The resulting equations correspond to the (2.1)–(2.3).

Appendix B. Derivation of Nu in ACRBC

Due to the cylindrical geometry of the convection system, the definition of Nu in ACRBC is slightly different from that in the classical RBC. Here we derive the expressions (2.5) of Nu . When there is only pure conduction between the hot and cold cylinders, the energy equation reads

$$\frac{d}{dr} \left(r \frac{d\theta}{dr} \right) = 0, \tag{B1}$$

and the boundary conditions, $\theta(R_i) = \theta_{cold}$, $\theta(R_o) = \theta_{hot}$, so we have the temperature profile along radial direction as

$$\theta = \theta_{cold} + (\theta_{hot} - \theta_{cold}) \frac{\ln(r/R_i)}{\ln(R_o/R_i)}, \tag{B2}$$

and consequently the heat flux by pure conduction,

$$J_{con} = -\chi \frac{d\theta}{dr} = \frac{\chi \Delta}{r \cdot \ln(\eta)}, \tag{B3}$$

where $\chi = \kappa \rho c_p$ is the thermal conductivity of the working fluid with ρ and c_p the density and the specific heat capacity of the fluid, $\Delta = \theta_{hot} - \theta_{cold}$ the temperature difference between the hot and cold cylinders and $\eta = R_i/R_o$. Besides, the temperature at the midradius position $R_i + (R_o - R_i)/2$ for pure thermal conduction state is

$$(\theta_c)_{cond} = -\frac{1}{\ln \eta} \ln[1/2 + 1/(2\eta)]. \tag{B4}$$

The thermal convection–diffusion equation reads

$$\frac{\partial \theta}{\partial t} + \mathbf{u} \cdot \nabla \theta = \kappa \nabla^2 \theta, \tag{B5}$$

and in cylindrical coordinates it reads

$$\frac{\partial \theta}{\partial t} + \frac{1}{r} \frac{\partial}{\partial r} \left(r \left(u_r \theta - \kappa \frac{\partial \theta}{\partial r} \right) \right) + \frac{1}{r} \frac{\partial}{\partial \varphi} \left(u_\varphi \theta - \frac{\kappa}{r} \frac{\partial \theta}{\partial \varphi} \right) + \frac{\partial}{\partial z} \left(u_z \theta - \kappa \frac{\partial \theta}{\partial z} \right) = 0. \tag{B6}$$

Averaging this equation azimuthally, axially and temporally, we obtain

$$\frac{1}{r} \frac{\partial}{\partial r} \left(r \left(\langle u_r \theta \rangle_{t,\varphi,z} - \kappa \frac{\partial}{\partial r} \langle \theta \rangle_{t,\varphi,z} \right) \right) = 0, \tag{B7}$$

meaning

$$r \left(\langle u_r \theta \rangle_{t,\varphi,z} - \kappa \frac{\partial}{\partial r} \langle \theta \rangle_{t,\varphi,z} \right) = \text{constant}. \tag{B8}$$

Hence the convective heat flux can be expressed as

$$J = \rho c_p \left(\langle u_r \theta \rangle_{t,\varphi,z} - \kappa \frac{\partial}{\partial r} \langle \theta \rangle_{t,\varphi,z} \right). \tag{B9}$$

Finally, using (B3) and (B9), we can define the Nu as

$$Nu = \frac{J}{J_{con}} = \frac{\langle u_r \theta \rangle_{t,\varphi,z} - \kappa \frac{\partial}{\partial r} \langle \theta \rangle_{t,\varphi,z}}{\kappa \Delta (r \cdot \ln(\eta))^{-1}}. \tag{B10}$$

Appendix C. Simulation parameters

No.	η	Ra	Δ_g/η_K	N_{iBL}	N_{oBL}	τ_{avg}	Nu	ϵ_{Nu}	Γ	ϕ_0	$N_\phi \times N_z \times N_r$
1	0.3	1.0×10^6	0.24	16	17	255	6.12	0.67 %	1	1	$1024 \times 128 \times 128$
2	0.3	2.2×10^6	0.31	13	12	152	7.68	1.09 %	1	1	$1024 \times 128 \times 128$
3	0.3	4.7×10^6	0.40	11	13	377	9.39	0.90 %	1	1	$1024 \times 128 \times 128$
4	0.3	1.0×10^7	0.51	12	17	247	11.41	0.79 %	1	1	$1024 \times 128 \times 128$
5	0.3	2.2×10^7	0.46	17	22	105	14.46	0.57 %	0.5	1/2	$960 \times 96 \times 192$
6	0.3	2.2×10^7	0.35	24	25	108	14.20	1.36 %	0.25	1/2	$1024 \times 64 \times 256$
7	0.3	4.7×10^7	0.58	15	17	181	17.88	0.15 %	0.5	1/2	$960 \times 96 \times 192$
8	0.3	1.0×10^8	0.57	18	19	101	22.37	1.26 %	0.25	1/2	$1024 \times 64 \times 256$
9	0.4	1.0×10^6	0.25	16	13	122	6.69	1.23 %	1	1	$1408 \times 128 \times 128$
10	0.4	2.2×10^6	0.32	14	16	282	8.42	0.70 %	1	1	$1408 \times 128 \times 128$
11	0.4	4.7×10^6	0.41	13	16	179	10.28	0.90 %	1	1	$1408 \times 128 \times 128$
12	0.4	1.0×10^7	0.53	11	13	1306	13.14	0.01 %	1	1	$1408 \times 128 \times 128$
13	0.4	2.2×10^7	0.47	16	19	205	15.88	0.60 %	0.5	1	$2112 \times 96 \times 192$
14	0.4	4.7×10^7	0.61	14	17	641	19.99	0.58 %	0.5	1	$2112 \times 96 \times 192$
15	0.4	1.0×10^8	0.59	17	23	136	23.95	1.51 %	0.5	1/2	$1280 \times 128 \times 256$
16	0.5	1.0×10^6	0.25	18	19	105	6.66	1.33 %	1	1	$1536 \times 128 \times 128$
17	0.5	2.2×10^6	0.40	11	13	521	8.28	0.49 %	1	1	$1212 \times 102 \times 102$
18	0.5	4.7×10^6	0.52	9	12	786	10.86	0.12 %	1	1	$1212 \times 102 \times 102$
19	0.5	1.0×10^7	0.54	11	13	200	13.54	0.20 %	1	1	$1536 \times 128 \times 128$
20	0.5	2.2×10^7	0.56	12	16	333	17.21	0.74 %	1	1	$1944 \times 162 \times 162$
21	0.5	4.7×10^7	0.62	13	17	540	21.79	0.25 %	0.5	1/2	$1152 \times 96 \times 192$
22	0.5	1.0×10^8	0.62	15	20	166	28.33	0.59 %	0.25	1/2	$1536 \times 64 \times 256$
23	0.5	1.0×10^8	0.62	15	20	711	28.04	1.45 %	1	1	$3072 \times 256 \times 256$
24	0.6	1.0×10^6	0.25	17	16	416	6.80	0.31 %	1	1/2	$1024 \times 128 \times 128$
25	0.6	2.2×10^6	0.33	15	16	381	8.52	0.05 %	1	1/2	$1024 \times 128 \times 128$
26	0.6	4.7×10^6	0.42	13	15	351	10.68	0.49 %	1	1/2	$1024 \times 128 \times 128$
27	0.6	1.0×10^7	0.55	11	13	654	13.56	0.21 %	1	1/2	$1024 \times 128 \times 128$

Table 1. For see caption on next page.

No.	η	Ra	Δ_g/η_K	N_{iBL}	N_{vBL}	τ_{avg}	Nu	ϵ_{Nu}	Γ	ϕ_0	$N_\phi \times N_z \times N_r$
28	0.6	2.2×10^7	0.49	15	20	341	17.40	1.05 %	1	1/2	$1536 \times 192 \times 192$
29	0.6	4.7×10^7	0.64	12	18	389	22.38	0.33 %	1	1/2	$1536 \times 192 \times 192$
30	0.6	1.0×10^8	0.63	15	21	305	29.35	0.14 %	0.25	1/4	$1024 \times 64 \times 256$
31	0.6	1.0×10^8	0.64	14	19	161	30.95	0.90 %	0.25	1/2	$2048 \times 64 \times 256$
32	0.7	1.0×10^6	0.25	17	20	714	6.90	0.06 %	1	1/4	$768 \times 128 \times 128$
33	0.7	2.2×10^6	0.33	15	17	528	8.63	0.47 %	1	1/4	$768 \times 128 \times 128$
34	0.7	4.7×10^6	0.42	13	16	711	10.74	0.07 %	1	1/4	$768 \times 128 \times 128$
35	0.7	1.0×10^7	0.56	10	14	664	14.48	0.36 %	1	1	$2560 \times 128 \times 128$
36	0.7	2.2×10^7	0.51	14	19	349	19.22	0.04 %	1	1/4	$1152 \times 192 \times 192$
37	0.7	4.7×10^7	0.65	12	16	439	24.29	1.19 %	1	1/4	$1152 \times 192 \times 192$
38	0.7	1.0×10^8	0.64	15	22	145	30.65	0.62 %	1	1/4	$1280 \times 256 \times 256$
39	0.8	1.0×10^6	0.39	10	12	1013	7.17	0.03 %	1	1	$2512 \times 82 \times 82$
40	0.8	2.2×10^6	0.50	8	10	678	9.13	0.04 %	1	1	$2512 \times 82 \times 82$
41	0.8	4.7×10^6	0.54	9	10	228	11.79	0.65 %	1	1	$3132 \times 102 \times 102$
42	0.8	1.0×10^7	0.56	10	13	461	15.05	0.13 %	1	1	$3968 \times 128 \times 128$
43	0.8	2.2×10^7	0.49	15	20	228	19.95	0.86 %	0.5	1/4	$1624 \times 102 \times 204$
44	0.8	4.7×10^7	0.62	12	18	249	25.06	0.46 %	0.5	1/4	$1624 \times 102 \times 204$
45	0.8	1.0×10^8	0.65	14	21	381	32.01	0.51 %	0.25	1/4	$2048 \times 64 \times 256$
46	0.9	1.0×10^6	0.26	17	19	199	7.31	1.73 %	1	1/8	$1024 \times 128 \times 128$
47	0.9	2.2×10^6	0.34	15	17	223	9.19	1.50 %	1	1/8	$1024 \times 128 \times 128$
48	0.9	4.7×10^6	0.44	12	17	233	11.80	1.36 %	1	1/8	$1024 \times 128 \times 128$
49	0.9	4.7×10^6	0.44	12	15	144	11.94	0.27 %	0.5	1/4	$2048 \times 64 \times 128$
50	0.9	1.0×10^7	0.56	10	13	178	15.29	0.94 %	1	1/4	$1984 \times 128 \times 128$
51	0.9	2.2×10^7	0.50	14	19	363	18.74	0.16 %	1	1/8	$1536 \times 192 \times 192$
52	0.9	4.7×10^7	0.65	12	19	499	23.70	0.23 %	1	1/8	$1536 \times 192 \times 192$
53	0.9	1.0×10^8	0.65	14	21	85	32.13	0.11 %	0.25	1/4	$4096 \times 64 \times 256$

Table 1. The columns from left to right indicate the following: radius ratio η , Rayleigh number Ra , the maximum grid spacing Δ_g compared with the Kolmogorov scale estimated by the global criterion $\eta_K = LPr^{1/2}/[Ra(Nu - 1)]^{1/4} \cdot [(1 + \eta) \ln(\eta)/2(\eta - 1)]^{1/4}$ (Jiang *et al.* 2020), the number of grid points within the thermal BL N_{iBL} and viscous BL N_{vBL} , the averaging time period τ_{avg} , Nusselt number Nu , the difference of Nu between inner and outer walls $\epsilon_{Nu} = |Nu_{in} - Nu_{out}|/Nu$, aspect ratio Γ , reduced azimuthal domain ϕ_0 , the resolution in azimuthal, axial, and radial directions $N_\phi \times N_z \times N_r$. Note that the azimuthal resolution corresponds to the resolution of the segment. For example, $N_\phi = 1024$ for $\phi_0 = 1/2$ means 1024 points for one half of the annulus.

REFERENCES

AHLERS, G., GROSSMANN, S. & LOHSE, D. 2009 Heat transfer and large scale dynamics in turbulent Rayleigh–Bénard convection. *Rev. Mod. Phys.* **81**, 503–537.

AZOUNI, M.A., BOLTON, E.W. & BUSSE, F.H. 1985 Convection driven by centrifugal buoyancy in a rotating annulus. *Geophys. Astrophys. Fluid Dyn.* **34** (1–4), 301–317.

BLOSS, A., ZHU, X., VERZICCO, R., LOHSE, D. & STEVENS, R.J.A.M. 2020 Flow organization and heat transfer in turbulent wall sheared thermal convection. *J. Fluid Mech.* **897**, A22.

BOHN, D., DEUKER, E., EMUNDS, R. & GORZELITZ, V. 1995 Experimental and theoretical investigations of heat transfer in closed gas-filled rotating annuli. *Trans. ASME J. Turbomach.* **117** (1), 175–183.

BUSSE, F.H. 1994 Convection driven zonal flows and vortices in the major planets. *Chaos* **4** (2), 123–134.

BUSSE, F.H. & CARRIGAN, C.R. 1974 Convection induced by centrifugal buoyancy. *J. Fluid Mech.* **62** (3), 579–592.

BUSSE, F.H. & OR, A.C. 1986 Convection in a rotating cylindrical annulus: thermal Rossby waves. *J. Fluid Mech.* **166**, 173–187.

Downloaded from https://www.cambridge.org/core. Tsinghua University, on 11 Nov 2021 at 10:50:50, subject to the Cambridge Core terms of use, available at https://www.cambridge.org/core/terms. https://doi.org/10.1017/jfm.2021.889

Effects of radius ratio on annular centrifugal convection

- CARDIN, P. & OLSON, P. 1994 Chaotic thermal convection in a rapidly rotating spherical shell: consequences for flow in the outer core. *Phys. Earth Planet. Inter.* **82** (3), 235–259.
- CHALGHOUM, I., ELAOU, S., KANFOUDI, H. & AKROUT, M. 2018 The effects of the rotor-stator interaction on unsteady pressure pulsation and radial force in a centrifugal pump. *J. Hydrodyn.* **30** (4), 672–681.
- CHEN, X., WANG, D.-P. & XI, H.-D. 2020 Reduced flow reversals in turbulent convection in the absence of corner vortices. *J. Fluid Mech.* **891**, R5.
- CHENG, L., ABRAHAM, J., HAUSFATHER, Z. & TRENBERTH, K.E. 2019 How fast are the oceans warming? *Science* **363**, 128–129.
- CHILLÀ, F. & SCHUMACHER, J. 2012 New perspectives in turbulent Rayleigh–Bénard convection. *Eur. Phys. J. E* **35** (7), 1–25.
- CHONG, K.L., YANG, Y., HUANG, S.-D., ZHONG, J.-Q., STEVENS, R.J.A.M., VERZICCO, R., LOHSE, D. & XIA, K.-Q. 2017 Confined Rayleigh–Bénard, rotating Rayleigh–Bénard, and double diffusive convection: a unifying view on turbulent transport enhancement through coherent structure manipulation. *Phys. Rev. Lett.* **119**, 064501.
- COURANT, R., FRIEDRICHS, K. & LEWY, H. 1928 Über die partiellen Differenzgleichungen der mathematischen Physik. *Math. Ann.* **100**, 32–74.
- CUSHMAN-ROISIN, B. & BECKERS, J.-M. 2011 The coriolis force. In *Introduction to Geophysical Fluid Dynamics*, chap. 2, pp. 42–45. Academic Press.
- FOWLIS, W.W. & HIDE, R. 1965 Thermal convection in a rotating annulus of liquid: effect of viscosity on the transition between axisymmetric and non-axisymmetric flow regimes. *J. Atmos. Sci.* **22**, 541–558.
- GASTINE, T., WICHT, J. & AURNOU, J.M. 2015 Turbulent Rayleigh–Bénard convection in spherical shells. *J. Fluid Mech.* **778**, 721–764.
- GOLUSKIN, D., JOHNSTON, H., FLIERL, G.R. & SPIEGEL, E.A. 2014 Convectively driven shear and decreased heat flux. *J. Fluid Mech.* **759**, 360–385.
- GROSSMANN, S., LOHSE, D. & SUN, C. 2016 High-Reynolds number Taylor–Couette turbulence. *Annu. Rev. Fluid Mech.* **48** (1), 53–80.
- VON HARDENBERG, J., GOLUSKIN, D., PROVENZALE, A. & SPIEGEL, E.A. 2015 Generation of large-scale winds in horizontally anisotropic convection. *Phys. Rev. Lett.* **115**, 134501.
- HARTMANN, D.L., MOY, L.A. & FU, Q. 2001 Tropical convection and the energy balance at the top of the atmosphere. *J. Clim.* **14** (24), 4495.
- HEIMPEL, M., AURNOU, J. & WICHT, J. 2005 Simulation of equatorial and high-latitude jets on Jupiter in a deep convection model. *Nature* **438**, 193–196.
- HUANG, S.-D., KACZOROWSKI, M., NI, R. & XIA, K.-Q. 2013 Confinement-induced heat-transport enhancement in turbulent thermal convection. *Phys. Rev. Lett.* **111**, 104501.
- HUANG, S.-D. & XIA, K.-Q. 2016 Effects of geometric confinement in quasi-2-D turbulent Rayleigh–Bénard convection. *J. Fluid Mech.* **794**, 639–654.
- JIANG, H., ZHU, X., MATHAI, V., VERZICCO, R., LOHSE, D. & SUN, C. 2018 Controlling heat transport and flow structures in thermal turbulence using ratchet surfaces. *Phys. Rev. Lett.* **120**, 044501.
- JIANG, H., ZHU, X., WANG, D., HUISMAN, S.G. & SUN, C. 2020 Supergravitational turbulent thermal convection. *Sci. Adv.* **6**, eabb8676.
- KANG, C., MEYER, A., YOSHIKAWA, H.N. & MUTABAZI, I. 2019 Numerical study of thermal convection induced by centrifugal buoyancy in a rotating cylindrical annulus. *Phys. Rev. Fluids* **4**, 043501.
- KING, M.P., WILSON, M. & OWEN, J.M. 2005 Rayleigh–Bénard convection in open and closed rotating cavities. *Trans. ASME J. Engng Gas Turbines Power* **129** (2), 305–311.
- KUNNEN, R.P.J., OSTILLA-MÓNICO, R., VAN DER POEL, E.P., VERZICCO, R. & LOHSE, D. 2016 Transition to geostrophic convection: the role of the boundary conditions. *J. Fluid Mech.* **799**, 413–432.
- LOHSE, D. & XIA, K.-Q. 2010 Small-scale properties of turbulent Rayleigh–Bénard convection. *Annu. Rev. Fluid Mech.* **42** (1), 335–364.
- MCKENZIE, D.P., ROBERTS, J.M. & WEISS, N.O. 1974 Convection in the earth’s mantle: towards a numerical simulation. *J. Fluid Mech.* **62** (3), 465–538.
- MICHAEL OWEN, J. & LONG, C.A. 2015 Review of buoyancy-induced flow in rotating cavities. *Trans. ASME J. Turbomach.* **137** (11), 111001.
- OBERBECK, A. 1879 Ueber die Wärmeleitung der Flüssigkeiten bei Berücksichtigung der Strömungen infolge von Temperaturdifferenzen. *Ann. Phys.* **243** (6), 271–292.
- OSTILLA, R., STEVENS, R.J.A.M., GROSSMANN, S., VERZICCO, R. & LOHSE, D. 2013 Optimal Taylor–Couette flow: direct numerical simulations. *J. Fluid Mech.* **719**, 14–46.
- PITZ, D.B., CHEW, J.W., MARXEN, O. & HILLS, N.J. 2017a Direct numerical simulation of rotating cavity flows using a spectral element-Fourier method. *Trans. ASME J. Engng Gas Turbines Power* **139** (7), 072602.

- PITZ, D.B., MARXEN, O. & CHEW, J.W. 2017*b* Onset of convection induced by centrifugal buoyancy in a rotating cavity. *J. Fluid Mech.* **826**, 484–502.
- VAN DER POEL, E.P., OSTILLA-MÓNICO, R., DONNERS, J. & VERZICCO, R. 2015*a* A pencil distributed finite difference code for strongly turbulent wall-bounded flows. *Comput. Fluids* **116**, 10–16.
- VAN DER POEL, E.P., STEVENS, R.J.A.M. & LOHSE, D. 2011 Connecting flow structures and heat flux in turbulent Rayleigh–Bénard convection. *Phys. Rev. E* **84**, 045303.
- VAN DER POEL, E.P., VERZICCO, R., GROSSMANN, S. & LOHSE, D. 2015*b* Plume emission statistics in turbulent Rayleigh–Bénard convection. *J. Fluid Mech.* **772**, 5–15.
- PORCO, C.C., *et al.* 2003 Cassini imaging of Jupiter’s atmosphere, satellites, and rings. *Science* **299**, 1541–1547.
- READ, P.L., MORICE-ATKINSON, X., ALLEN, E.J. & CASTREJÓN-PITA, A.A. 2017 Phase synchronization of baroclinic waves in a differentially heated rotating annulus experiment subject to periodic forcing with a variable duty cycle. *Chaos* **27** (12), 127001.
- READ, P.L. & RISCH, S.H. 2011 A laboratory study of global-scale wave interactions in baroclinic flow with topography I: multiple flow regimes. *Geophys. Astrophys. Fluid Dyn.* **105** (2–3), 128–160.
- RHINES, P.B. 1975 Waves and turbulence on a beta-plane. *J. Fluid Mech.* **69** (3), 417–443.
- ROUHI, A., LOHSE, D., MARUSIC, I., SUN, C. & CHUNG, D. 2021 Coriolis effect on centrifugal buoyancy-driven convection in a thin cylindrical shell. *J. Fluid Mech.* **910**, A32.
- SILANO, G., SREENIVASAN, K.R. & VERZICCO, R. 2010 Numerical simulations of Rayleigh–Bénard convection for Prandtl numbers between 10^{-1} and 10^4 and Rayleigh numbers between 10^5 and 10^9 . *J. Fluid Mech.* **662**, 409–446.
- SUN, C., REN, L.-Y., SONG, H. & XIA, K.-Q. 2005 Heat transport by turbulent Rayleigh–Bénard convection in 1 m diameter cylindrical cells of widely varying aspect ratio. *J. Fluid Mech.* **542**, 165–174.
- VERZICCO, R. & ORLANDI, P. 1996 A finite-difference scheme for three-dimensional incompressible flows in cylindrical coordinates. *J. Comput. Phys.* **123**, 402–414.
- WANG, C., JIANG, L., JIANG, H., SUN, C. & LIU, S. 2021 Heat transfer and flow structure of two-dimensional thermal convection over ratchet surfaces. *J. Hydrodyn.* **33** (5), 93–103.
- WANG, Q., CHONG, K.L., STEVENS, R.J.A.M., VERZICCO, R. & LOHSE, D. 2020 From zonal flow to convection rolls in Rayleigh–Bénard convection with free-slip plates. *J. Fluid Mech.* **905**, A21.
- WILLIAMS, G.P. 1971 Baroclinic annulus waves. *J. Fluid Mech.* **49** (3), 417–449.
- WU, X.-Z. & LIBCHABER, A. 1991 Non-Boussinesq effects in free thermal convection. *Phys. Rev. A* **43**, 2833–2839.
- WYNGAARD, J.C. 1992 Atmospheric turbulence. *Annu. Rev. Fluid Mech.* **24** (1), 205–234.
- XIA, K.-Q. 2013 Current trends and future directions in turbulent thermal convection. *Theor. Appl. Mech. Lett.* **3** (5), 052001.
- YANO, J.-I., TALAGRAND, O. & DROSSART, P. 2005 Deep two-dimensional turbulence: an idealized model for atmospheric jets of the giant outer planets. *Geophys. Astrophys. Fluid Dyn.* **99** (2), 137–150.
- YIK, H., VALORI, V. & WEISS, S. 2020 Turbulent Rayleigh–Bénard convection under strong non-Oberbeck-Boussinesq conditions. *Phys. Rev. Fluids* **5**, 103502.
- YU, Y., LIU, F., ZHOU, T., GAO, C. & LIU, Y. 2019 Numerical solutions of 2-D steady compressible natural convection using high-order flux reconstruction. *Acta Mechanica Sin.* **35**, 401–410.
- ZHANG, J., CHILDRESS, S. & LIBCHABER, A. 1997 Non-Boussinesq effect: thermal convection with broken symmetry. *Phys. Fluids* **9** (4), 1034–1042.
- ZHANG, Y., ZHOU, Q. & SUN, C. 2017 Statistics of kinetic and thermal energy dissipation rates in two-dimensional turbulent Rayleigh–Bénard convection. *J. Fluid Mech.* **814**, 165–184.
- ZHU, X., *et al.* 2018 AFiD-GPU: a versatile Navier–Stokes solver for wall-bounded turbulent flows on GPU clusters. *Comput. Phys. Commun.* **229**, 199–210.
- ZOU, H.-Y., ZHOU, W.-F., CHEN, X., BAO, Y., CHEN, J. & SHE, Z.-S. 2019 Boundary layer structure in turbulent Rayleigh–Bénard convection in a slim box. *Acta Mechanica Sin.* **35**, 713–728.